Extreme-ultraviolet Late Phase Caused by Magnetic Reconnection over Quadrupolar Magnetic Configuration in a Solar Flare

Zhenjun Zhou (周振军)[1,6] , Xin Cheng[2,3] , Lijuan Liu[1] , Yu Dai[2,3] , Yuming Wang[4,5] , and Jun Cui[1]

[1] School of Atmospheric Sciences, Sun Yat-sen University, Zhuhai, Guangdong, 519000, People's Republic of China; zhouzhj7@mail.sysu.edu.cn
[2] School of Astronomy and Space Science, Nanjing University, Nanjing 210093, People's Republic of China
[3] Key Laboratory for Modern Astronomy and Astrophysics (Nanjing University), Ministry of Education, Nanjing 210093, People's Republic of China
[4] CAS Key Laboratory of Geospace Environment, Department of Geophysics and Planetary Sciences, University of Science and Technology of China, Hefei, Anhui 230026, People's Republic of China
[5] Synergetic Innovation Center of Quantum Information & Quantum Physics, University of Science and Technology of China, Hefei, Anhui 230026, People's Republic of China

Abstract

A second emission enhancement in warm coronal extreme-ultraviolet (EUV) lines (about 2–7 MK) during some solar flares is known as the EUV late phase. Imaging observations confirm that the late-phase emission originates from a set of longer or higher loops than the main flare loops. Nevertheless, some questions remain controversial: What is the relationship between these two loop systems? What is the heating source of late-phase emission? Does heating accompany the main-phase heating or does it occur quite later? In this paper, we present clear evidence for a heating source in a late-phase solar flare: magnetic reconnection of the overlying field in a quadrupolar magnetic configuration. The event is triggered by an erupted core structure that eventually leads to a coronal mass ejection. A cusp feature and its shrinkage motion high in the late-phase emission region are manifestations of the later phase reconnection following the main flare reconnection. Using the enthalpy-based thermal evolution of loops model, we reasonably reproduce the late-phase emissions in some EUV lines. We suggest that continuous additional heating is responsible for the appearance of the elongated EUV late phase.

Key words: Sun: corona – Sun: flares – Sun: UV radiation

Supporting material: animation

1. Introduction

A solar flare, localized brightening in the solar atmosphere, rapidly releases radiation over a wide range of the electromagnetic spectrum. Besides the radiation enhancement, sometimes the flare also accelerates high energy particles and is accompanied with magnetic flux ejected into the interplanetary space, which is manifested as a coronal mass ejection (CME).

Solar flares are generally believed to be a result of magnetic reconnection—the merging of antiparallel magnetic fields and the consequent release of magnetic energy. The free magnetic energy is convert into the kinetic energy of the CME and significant particle acceleration and plasma heating. When the impulsive flare heating is terminated, the plasma will cool down mainly by conduction and radiation. Initially, the energy is transported downward mainly in the form of conductive flux or nonthermal particles and deposited in the transition region (TR) and chromosphere. Due to the Coulomb collisions, heating, and strong ablation, the ambient chromospheric plasma is strongly heated and expands upward, filling the coronal loops, known as the chromospheric evaporation (Antiochos & Sturrock 1978). As the loop temperature decreases and the density increases, radiation gradually becomes dominant. As the plasma cools, pressure gradients drop to subhydrostatic values, and material drains from the corona (Klimchuk et al. 2008).

Observations show that flares typically experience three stages: (1) a precursor phase, presenting a small emission enhancement at radio, Hα, UV to extreme-ultraviolet (EUV) wavelengths (e.g., Bumba & Krivský 1959; Martin 1980; Van

Hoven & Hurford 1984; Cheng et al. 1985; Warren & Warshall 2001; Contarino et al. 2003; Fárník et al. 2003); (2) an impulsive phase indicated by rapid enhancement of a microwave burst and/or a hard X-ray burst that lasts from 100 to 1000 s in which protons and electrons are accelerated to energies over 1 MeV; and (3) a decay phase that lasts for several minutes or hours with the gradual increase and decrease of soft X-ray and EUV emissions (Hudson 2011, and reference therein).

However, recent observations revealed that in some solar flares, warm coronal emission lines (about 2–7 MK) exhibit a second emission peak (Woods et al. 2011) as seen by the EUV Variability Experiment (EVE; Woods et al. 2012) on board the *Solar Dynamics Observatory* (*SDO*; Pesnell et al. 2012). This secondary peak, referred to as the late phase and not subject to any stages mentioned above, lags behind the *GOES* X-ray peak for tens of minutes to hours. Woods et al. (2011) proposed four observational criteria to define an EUV late phase: (1) a second peak in the warm emissions (e.g., Fe XV and Fe XVI) after the *GOES* soft X-ray peak; (2) no significant enhancements in hot emissions (e.g., Fe XX) during the second peak; (3) association with an eruptive event seen in imaging observations; and (4) the existence of a second set of higher and longer loops relative to the main flaring loops. In general, the emission of an EUV late-phase flare is from the synthesis effect of thermal evolution from these two sets of loop systems. The difference in cooling rate between different loops could discriminate the two peaks in warm coronal emission lines (Liu et al. 2013a; Wang et al. 2016). Yet, the cooling process of another longer loop alone cannot be sufficient for some long delay (several hours) cases (Hock et al. 2012).

---

[6] Contributing author.

Nevertheless, how the late-phase loop system is heated up is still unknown. Studies have explored the possibility of additional heating (Woods et al. 2011; Hock et al. 2012; Dai et al. 2013; Sun et al. 2013), as well as the long-lasting cooling timescale (Liu et al. 2013a; Sun et al. 2013). Using the enthalpy-based thermal evolution of loops (EBTEL) model (Klimchuk et al. 2008; Cargill et al. 2012), Dai & Ding (2018) numerically simulated EUV late-phase flares under two main mechanisms, i.e., long duration plasma cooling and additional heating mechanisms. They found that the late-phase peak occurs during the radiative cooling phase of the late-phase loop if it is a long-lasting cooling process, while the additional heating probably makes the late-phase peak take place in the conductive cooling phase. They proposed that the shape of late-phase light curves can be used to differentiate the two mechanisms.

Meanwhile, statistical analysis (Woods et al. 2011) showed that the flares with late phases exhibit clustering phenomena in certain active regions (ARs), implying a specific magnetic configuration of the ARs in which EUV late-phase flares are preferentially produced. From direct EUV imaging observation, the basic 2D configuration of the magnetic topology is considered as a quadrupolar configuration—a typical symmetric (Hock et al. 2012) or asymmetric (Liu et al. 2013a) quadrupolar configuration. In reality, ARs often show a more complicated configuration. Sun et al. (2013) considered a fan-spine topology with a closed-field configuration, in which the late-phase peak comes from the cooling of large post-reconnection loops beside and above the compact fan. This magnetic field configuration has been further verified through observation (Dai et al. 2013; Li et al. 2014; Masson et al. 2017). The key ingredients pertinent to AR magnetic configuration with late phase can be simply summarized as a quadrupolar configuration. This kind of topology distinguishes two sets of loop systems—the external late-phase loop system and inner main-phase loop system. Sun et al. (2013) suggested that the two systems and their evolutional trends are closely linked by the fan-spine topology in their case, while Hock et al. (2012) considered that these two loop systems have no direct linkage and that it is the CME that stretches the late-phase loops to reconnect. In both cases, during the late-phase stage, cusp-shaped structures are found above the main flare region, which is characteristic for ongoing reconnection behind ejecta. Particularly, when considering additional heating, the quantitative results are more consistent with observations (Sun et al. 2013).

Based on the above, the mechanism causing the late phase is still under debate. In this paper, we study a limb flare event with a well-defined EUV late phase. In Section 2, we introduce the instruments. In Section 3, we present observations and an analysis of the event, which are followed by an EBTEL modeling of the late-phase emission in Section 3.4. Finally, we present a summary and conclusion in Section 4.

2. Instruments

The data presented in this work primarily come from the Atmospheric Imaging Assembly (AIA; Lemen et al. 2012), which images the coronal plasma through six different EUV passbands. Among them, the 13.1 nm (Fe XXI, $\sim$10 MK), 9.4 nm (Fe XVIII, $\sim$6.4 MK), and 33.5 nm passbands (Fe XVI, $\sim$2.5 MK) are sensitive to hot (warm) plasma and can be used for thermal evolution analysis, and the other three passbands,

21.1 nm (Fe XIV, $\sim$2.0 MK), 19.3 nm (Fe XII, $\sim$1.6 MK), and 17.1 nm (Fe IX, $\sim$0.7 MK) are largely sensitive to plasma cooler than 2.0 MK, e.g., bulk coronal plasma. The cadence of these EUV images is 12 s and the pixel size is 0″.6. Note that the AIA 13.1 nm passband also includes Fe VIII lines that are expected to brighten up at relatively low coronal temperatures ($\sim$0.4 MK), and the AIA 19.3 nm passband contains a hot spectral line Fe XXIV ($\sim$20 MK; Lemen et al. 2012). The twin spacecraft of the *Solar Terrestrial Relationships Observatory* (*STEREO*; Kaiser et al. 2008) provide simultaneous multi-viewpoints from other two places. During the event, *STEREO* Ahead and Behind are about 157° west and 165° east from the Sun–Earth line along the ecliptic orbit around the Sun, while the *SDO* is situated near the Earth. The Extreme Ultraviolet Imager (EUVI) on the two *STEREO* spacecraft observe the chromosphere and low corona in four EUV passbands, which enables us to reconstruct the 3D shape of coronal loops using the triangulation technique. Here we choose the 19.5 nm (Fe XII, $\sim$1.5 MK) passbands from EUVI_A,B and 19.3 nm (Fe XII, $\sim$1.6 MK) passbands from *SDO*/AIA to display the evolution of the coronal loop from different angles and reconstruct their geometrical configuration. We use wavelet-enhanced images of *STEREO* EUVI provided by the Johns Hopkins University Applied Physics Laboratory. This image-processing technique (wavelet-enhanced) gives better visual clarity than the standard EUVI images (Stenborg et al. 2008).

Moreover, we make use of EVE observations, which obtain integrated emission from the Sun over a wide wavelength range (0.1–105 nm) with an unprecedented spectral resolution of 0.1 nm, high temporal cadence (10 s), and accuracy of 20% (Woods et al. 2012). EVE provides two set of level 2 data products including the "line" (EVL) product and the "spectra" (EVS) product, which are publicly available at http://lasp.colorado.edu/eve/data_access/evewebdataproducts/level2/.

3. Observations and Results

3.1. Overview of the Event

On 2014 April 25, a solar flare started at 00:17 UT and lasted over eight hours according to the *GOES* soft X-ray (SXR) flux (Figure 1(a)). The SXR flux (1–8 Å) reached a maximum of 1.3×10^{-4} Wm^{-2}, revealing an X1.3 class flare. At the time as the flare, the associated AR NOAA 12035 was located behind the west limb of the Sun. The accompanied CME had an initial speed around 600 km s^{-1} at a height of $\sim$3R_s. However, the velocity decreased to 300 km s^{-1} when the CME reached 20 R_s according to the CME catalog[7] based on the Large Angle Spectroscopic Coronagraph C2 and C3 observation (LASCO; Brueckner et al. 1995). Despite the fact that at that time the magnetic field of the AR cannot be measured, the magneto-grams recorded three days prior to the eruption revealed a quadrupolar magnetic configuration on the photosphere. The onset of the event was believed to be caused by breakout reconnection (Chen et al. 2016).

3.2. Extremely Large EUV Late Phase

Three emission lines from the EVL data are selected to study the EUV evolution of this event with the wavelength centered at 13.3 nm (Fe XX, $\sim$10 MK), 94 nm (Fe XVIII, $\sim$6.5 MK), and 33.5 nm (Fe XVI, $\sim$2.5 MK). These three EVE lines have

---

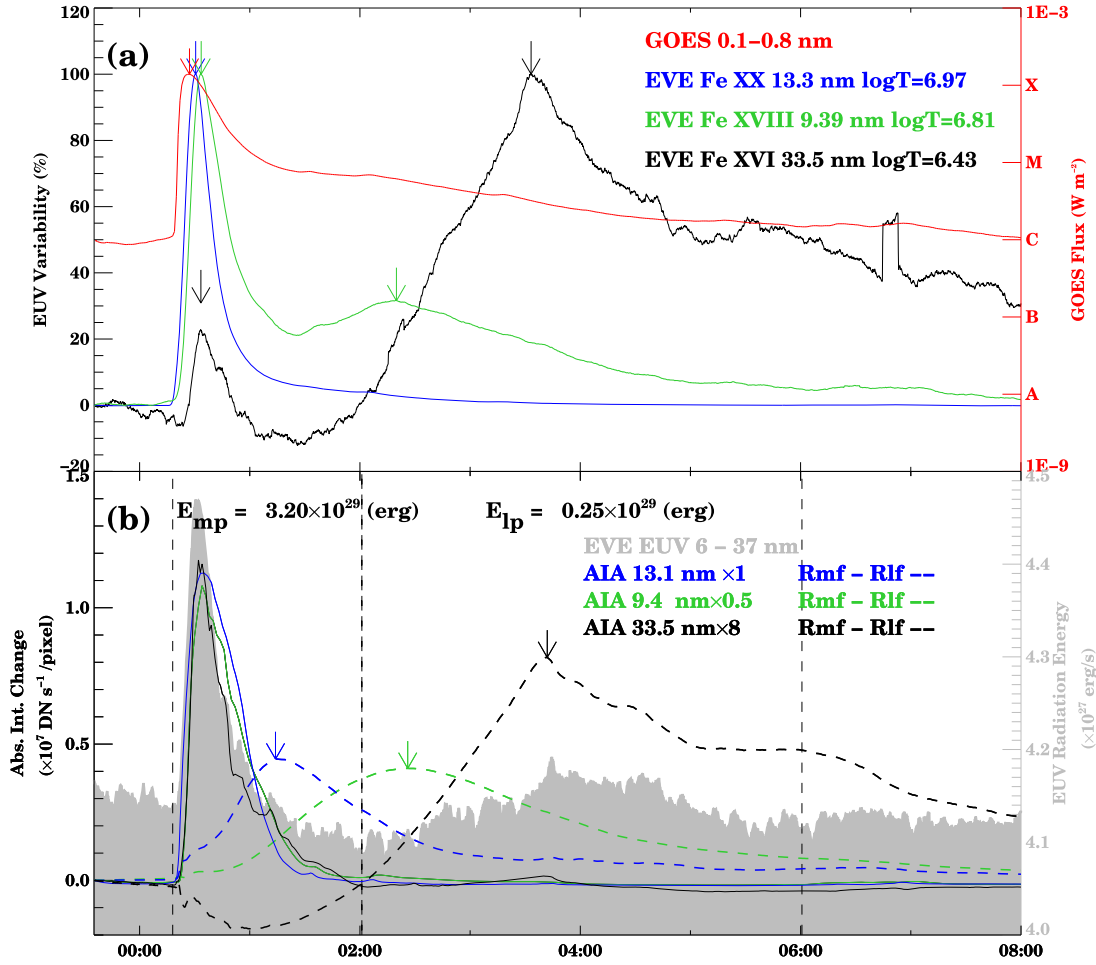[7] http://cdaw.gsfc.nasa.gov/CME_list

Figure 1. Time profiles of each channel for the 2014 April 25 X1.3 flare. Panel (a) shows the background-subtracted irradiance in three EVE lines (normalized) and *GOES* 0.1–0.8 nm flux. Panel (b) gives light curves from regions indicated by the boxes in Figure 2, with the total EUV radiative energy-loss rate overplotted. The dashed lines come from the large box region in Figure 2(i) and solid lines from the small box. The color-coded arrows denote the peak time for the corresponding emission.

complementary imaging observations from AIA. Subtracting the emission several minutes before the eruption, the temporal profiles of irradiance variability (normalized) in these lines during the flare period are plotted as blue, green, and black curves in Figure 1(a), respectively. The intensities of three EVE lines almost simultaneously enhance with the *GOES* SXR flux. The delay of the first peak (as pointed by the colored arrow) indicates the cooling process of the flare's main phase. Unlike the only peak in *GOES* SXR and 13.3 nm profile, a second peak appears in 9.4 and 33.5 nm. The intervals between the two peaks in 9.4 and 33.5 nm are 106 and 180 minutes, respectively. These secondary emission peaks in warm EUV lines (about 2–7 MK) are signatures of the EUV late phase. Furthermore, in the warm 33.5 nm line profile, the second peak is much stronger than the first peak, indicative of an extremely large EUV late phase (Liu et al. 2015). The flux ratio of the second peak to the first peak is around 5, much higher than the average value of 0.8 in statistics (Woods et al. 2011).

The EVS spectral data from the MEGS-A instrument provide continuous measurements for spectrum irradiance variability of the flare within the wavelength range of 6–37 nm. Here, the routine eve_integrate_line.pro from the SolarSoftware (SSW) package is employed to integrate irradiance over this

wavelength range using the midpoint rule:

$$E(t) = K \sum_{\lambda_{\min}}^{\lambda_{\max}} \Delta\lambda I_\lambda(t), \qquad (1)$$

where $\Delta\lambda$ is the wavelength bin and K is a conversion factor $(=10^7 \times 2 \times \pi \times (1\ \mathrm{au})^2)$ that transforms the irradiance flux in units of J m^{-2} at 1 au to the radiative loss rate in units of erg s^{-1} at the Sun assuming a uniform angular distribution of flare energy release (Woods et al. 2006). The radiative energy-loss rate in this EUV range is calculated according to Equation (1) (Liu et al. 2015) and displayed by the shaded area in Figure 1(b). It is interesting to note that there are also two peaks in the profile of the EUV radiative energy-loss rate. The vertical dashed lines bound the impulsive and the gradual phases from the two enhancements of Fe XVI 33.5 nm line irradiance, the former is from the onset of the impulsive phase at 00:17 UT to its conclusion at 02:00 UT, the latter includes the late-phase EUV enhancement between 02:00 UT and 06:00 UT. We also calculate the total flare EUV output in these two periods by simply integrating the emission with the background emission subtracted. In spite of a higher late-phase peak in the 33.5 nm line, the EUV radiation output releases much less

energy (0.25×10^{29} erg) during the flare late phase than that (3.2×10^{29} erg) during the flare main phase.

We turn to imaging observation such as *SDO*/AIA and *STEREO*/EUVI. The AIA instrument provides the corresponding imaging observations at 13.1, 9.4, and 33.5 nm. After checking the source region, we select a region restricted to a small region (Figure 2(h)) where emission is mainly caused by the main flaring loops and a larger region mainly responsible for the emission of the late phase. The regions are depicted as boxes in Figure 2(h), over which the intensity profiles at different channels are plotted in Figure 1(b). Obviously, the light curves from the main-phase region (solid lines) behave in a similar way—they rise up, reach the peak, and recover to the background nearly synchronously. The very close peak times of 13.1 nm (10 MK) to 33.5 nm (2.5 MK) signify a rapid cooling process of the main phase. In contrast, the brightness of the late-phase region (dashed lines in Figure 1(b)) shows a much more gradual evolution. The delay time is 56 minutes for the AIA 13.1 nm, 128 minutes for AIA 9.4 nm, and 204 minutes for AIA 33.5 nm (Table 1). There also appears a dimming from 00:17 to 02:00 UT at the 33.5 nm (Figure 1(b), blue dashed line) due to depletion of plasma density in areas associated with eruptions. These observations coincide with the previous conclusion that two sets of loop systems exist in the active region. Different from the compact loop system for the flare main phase, the late phase originates from another set of higher and longer loops.

Chen et al. (2016) analyzed the morphology of this case in detail and argued that the overall configuration of the AR is a quadrupolar magnetic configuration. Figure 2 shows the evolution of the eruption from different viewing angles during different stages with a pseudo 3D schematic at the bottom. Here all the images have been rotated with the eruption direction toward the top in order to compare with the cartoon. STEREO_A EUVI 19.5 nm provides the disk observation (Figures 2(a)–(c)), STEREO_B 19.5 nm (Figures 2(d)–(f)) and *SDO* 9.4 nm (Figures 2(g)–(i)) provide limb views. Two sidelobe structures can be easily identified at the AIA 9.4 nm channel, indicating hot structures similar to the bipolar configuration on both sides of Figure 2(j)'s cartoon. During the flare's main phase, a core structure expands outward, pushes the sidelobes aside, and finally erupts into the interplanetary space as seen in hot channels (like AIA 9.4 nm in Figures 2(g), (h), Figure 3 and the accompanied animation). The cartoon in Figure 2(k) depicts this scenario, but the low temperature coverage of EUVI 19.5 nm channel makes it only possible to see the brightness of the post flare loops (PFLs), with their footpoints marked as P1 and P2. When it comes to the late-phase stage, a totally different loop system appears, much longer and higher loops form with remote footpoints labeled as P3 and P4 (Figures 2(c) and (f)). Figure 2(i) shows the hot part of these loops in the top region. From Figure 1(b) we know that the emission of the late phase mainly comes from the big box region, namely the late-phase loop system. The late-phase loop system is often considered as a pre-existing structure somehow connected magnetically with the main-phase loop (Liu et al. 2013a; Sun et al. 2013), but our observation seems to be in favor of another scenario—the late-phase loop system comes from the newly reconnected large-scale arcades as the overlying field above the quadrupolar configuration is stretched by the erupting CME and then reconnects as shown by Figure 2(i) (Hock et al. 2012).

3.3. Late Phase Loop Evolution

This event presents a novel perspective to the origin of the EUV late phase. Interestingly, unusually large and hot overlying arcades appear above the flare after the CME eruption, as seen from the AIA view (Figure 3(a)). This structure is invisible in the low temperature wavelengths like AIA 19.3 nm and EUVI_B 19.5 nm. Cusp-shaped loops appeared at the top of the arcades that rapidly retreat sunward, and continuously pile up above the arcade (see Figure 3(a) and the accompanying animation). As these overlying arcades cool down, numbers of loops sequentially show up from the lower part to the higher part (Figure 3(d)) at the AIA 19.3 nm passband. Due to a strong cold line (Fe VIII, 0.4 MK) blending, the AIA 13.1 nm passband also shows cold loops during the cooling process (Figure 3(c)). Based on the morphology analysis in multiple temperatures, the evolution of the late-phase loop system experienced three stages: the initial stage, characterized by relatively low temperature high-lying arcades over the flare region (Figure 2(j)); the eruptive stage, similar to the classical flare magnetic reconnection scenario, in which the erupting CME stretches the overlying field, whose legs seem to curve-in toward the reconnection site; and the recovery stage, seen as the shrinkage of cusp structure in the high temperature channel (Figure 3(a)), which is commonly considered as X-type configuration, as sketched by Figure 2(i).

To further investigate the evolution of the late-phase loop system, we perform a quantitative analysis. Here we study two evolutions: the shrinkage motion and cooling process of the late-phase loops. We draw three slits: Slit S1 in Figure 3(a) is located at the cusp location, while S0 in Figure 2(f) and S2 in Figure 3(c) indicate that the eruption directions are used to trace late-phase loops. Figures 4(a), (b), and (c) are the slice–time stacking plots of slit S2 at the AIA 13.1, 9.4, and 33.5 nm passbands. A bright core region appears in all of these channels with its height above 50 Mm. The time delay of the brightness from 13.1 to 33.5 nm indicates the cooling of the overlying arcades. The vertical arrow in each channel gives the timing of the maximum intensity. When the temperature reaches a low level (such as 1 MK), in the slice–time diagram of slit S2 from AIA 19.3 nm channel and slit S0 from EUVI 19.5 nm channel, a bright feature slowly rises up with a fitting speed of $3.26 \mathrm{~km~s^{-1}}$. For PFLs, it is generally recognized that this kind of rising motion is an apparent ascending of these overlying loops instead of real mass motion. Here for the late-phase loops, we think that the same process could explain this motion. From Figure 4 and its accompanying animation one can see that the late-phase loops behave in a similar manner as PFLs, i.e., the newly reconnected loops continuously accumulate above the flare loops. So this gives us a hint that the duration of the brightness in each channel has direct correlation with the numbers of the shrinkage loops.

In Figure 4(d), a series of dark features continuously drop down toward to the flare loop top. These voids known as supra-arcade downflows (SADs) were first observed by Yohkoh SXT and TRACE (e.g., McKenzie & Hudson 1999; Gallagher et al. 2002) and SADs are closely related to the outflows produced by magnetic reconnection occurring high in the corona. Thus the dark features could be a consequence of newly reconnected loops. We identify the obvious trajectories of three dark features to trace the shrinkage motion. The velocities range from 97 to $143 \mathrm{~km~s^{-1}}$. The intervals between the neighboring stripes are 11.2 and 11.3 minutes in the AIA 13.1 nm slice–time
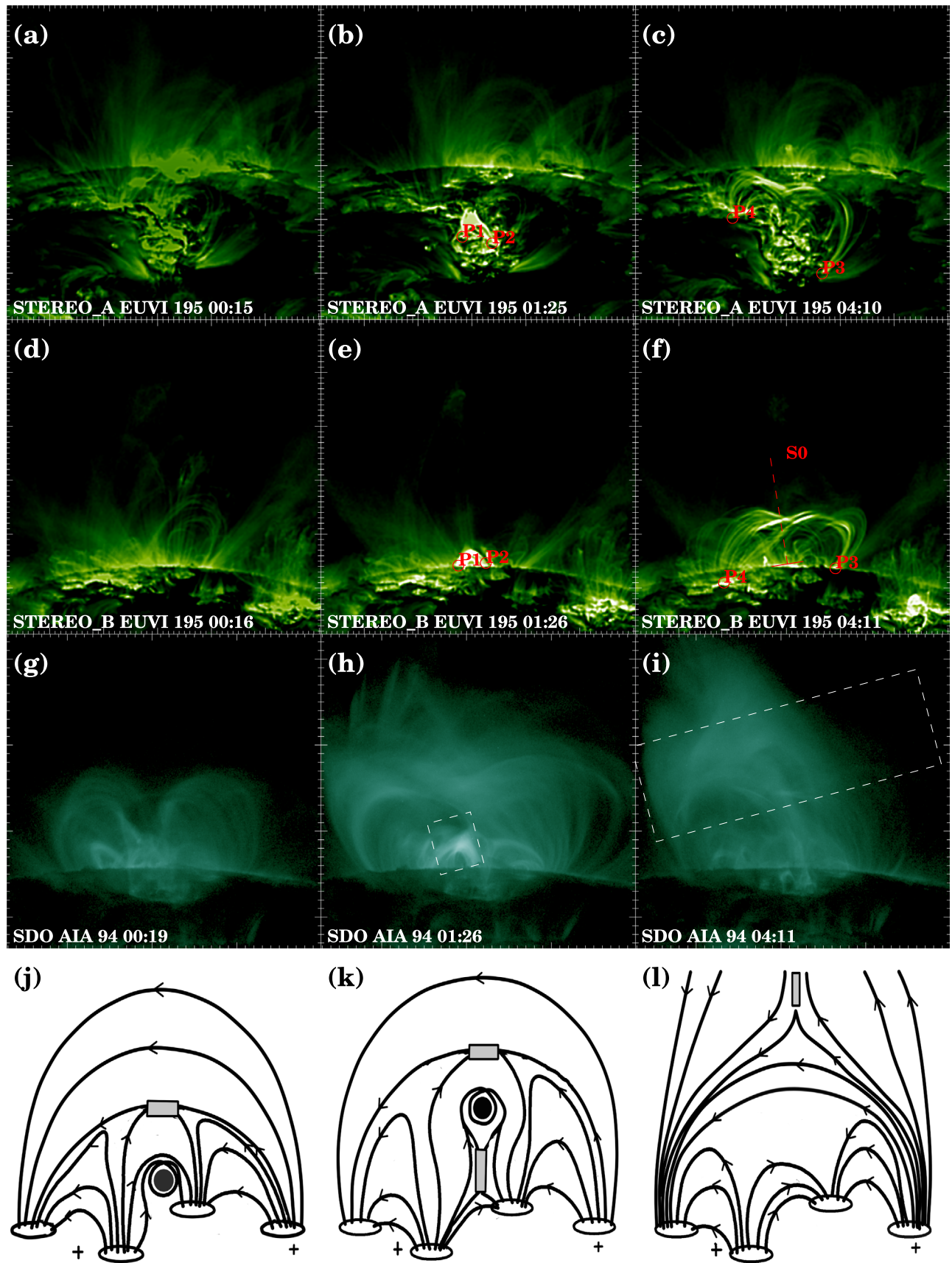
Figure 2. Three stages of this solar flare from different viewing angles. The first three rows are the observations from EUVI_A 19.5 nm, EUVI_B 19.5 nm, and AIA 9.4 nm, respectively. The last row shows schematic interpretation. All the observations are rotated with the eruption direction pointing to the top. The first column ((a), (d), (g), and (j)) shows the initial phase of the solar flare. The middle column displays the main phase and the last column displays the late phase. The cartoon images (j), (k), and (l) are adapted from Sterling & Moore (2004).

Table 1
Properties of the EUV Light Curves of the 2014 April 25 X1.3 Flare[a]

Line/Passband (nm)	Ion	Temperature (MK)	Peak Time (UT)		Delay Time (minutes)	
			Main Phase	Late Phase	Main Phase	Late Phase
SXR (0.1–0.8)	*	>10	00:27:10	*	10	*
MEGSA (6–37)	*	*	00:30:32	03:44:32	13	207
13.3	Fe XX	10	00:30:32	*	13	*
9.4	Fe XVIII	6.5	00:33:32	02:19:52	16	122
33.5	Fe XVI	2.5	00:33:22	03:33:12	16	196
13.1[a]	Fe XXI	10	00:35:00	01:14:00	18	57
9.4[a]	Fe XVIII	6.4	00:34:00	02:26:02	17	129
33.5[a]	Fe XVI	2.5	00:32:00	03:42:00	15	205

Note.
[a] In this table, the delay time is calculated from peak time to start time (00:17 UT) of the eruption. Superscript "a" indicates the light curve from the integrated average over the area of the respective box in the AIA image. The AIA 13.1 nm passband also contains a cold line (Fe VIII, 0.4 MK), in this study, the enhanced emission should be from the hot plasma during its peak time.

stacking plot of Figure 4(d), respectively. These stripes manifest the trajectories of SADs, which could be due to the SADs retract from the reconnection sites high in the corona and continuously cool down, giving rise to consecutive brightness in the different AIA channels.

To quantify the loop length of the single late-phase loop of the later simulation, we used the IDL routine scc_measure.pro in SSW to trace out the path of the loop in 3D space (Thompson 2009; Zhou et al. 2017). Because *STEREO* EUVI_A/B only have cool lines, we use the EUVI 19.5 nm (∼1.5 MK) and AIA 19.3 nm (∼1.6 MK) to reconstruct the loop. Both images in the AIA 19.3 nm and EUVI 19.5 nm at 04:10 UT show multiple clear bright loops. We select a loop and obtain its loop half length of 138 Mm. Its initial length should be larger because it has retracted before it becomes visible.

3.4. EBTEL Modeling of the Late-phase Emissions with Additional Heating

There are two major explanations for the EUV late phase: one is additional heating, and the other is long-lasting cooling. A definite answer perhaps requires modeling of a multitude of loops based on observations (e.g., Hock et al. 2012; Qiu et al. 2012; Liu et al. 2013b). Here, from possible signatures of the reconnection in the high corona, we take a heuristic approach with additional heating to model the late phase. The EBTEL-based flare model (Hock et al. 2012) is employed to simulate radiative output of the late-phase loop system. This model uses multiple EBTEL loops (e.g., 22 EBTEL loops) with variable loop lengths and heating rate profiles to synthesize the light curves of several EUV lines as measured by EVE, 13 out of 22 loops are employed to model the late-phase emissions. Here we use 10 EBTEL loops to model the late-phase radiative output.

3.4.1. The EBTEL Model

For a single EBTEL loop, its evolution can be controlled by loop-averaged equation of continuity and energy (Klimchuk et al. 2008; Cargill et al. 2012):

$$\frac{dn}{dt} = -\frac{c_2}{5c_3 k_B T}\left[\frac{F_c}{L} + c_1 n^2 \Lambda(T)\right], \qquad (2)$$

and

$$\frac{dP}{dt} = \frac{2}{3}[Q(t) - (1 + c_1)n^2\Lambda(T)], \qquad (3)$$

where n, P, and T are the mean density, pressure, and temperature of the loop, respectively, which follow from the equation of state, $P = 2nk_B T$ with k_B being the Boltzmann constant, c_2 (=0.9) is the typical ratio of average to apex temperature of a coronal loop, c_3 (=0.6) is the ratio between coronal base temperature and apex temperature, $Q(t)$ is the volumetric heating rate, $\Lambda(T)$ is the optically thin radiative loss function, $F_c = -(2/7)\kappa_0(T/c_2)^{7/2}/l$ (l the half loop length) is the thermal conductive flux, and c_1 is the ratio of radiative loss rate of the TR to that of the corona.

In addition, we only consider thermal heating $Q(t)$ and ignore nonthermal electron beam heating. The rationality of predigestion mainly relies on the following reasons. In the additional heating scenario, the nonthermal heating is unlikely to be the major heating source during the late phase based on the previous study that the late-phase arcades do not show obvious HXR emission (e.g., Li et al. 2012, 2014; Sun et al. 2013). In fact, Li et al. (2014) checked the effect of nonthermal beam heating using a flux for which the total energy was comparable to that of thermal heating, and found that the nonthermal effect is not significant in the EUV late phase. Thermal heating primarily raises the temperature of the coronal plasma, where nonthermal beam heating primarily raises the density. Liu et al. (2013b) discussed that the increased density caused by the nonthermal beam could somewhat enhance the EUV late-phase emission, but it affects the timing of the EUV late phase much less than a loop length variation. Meanwhile, we only calculate the emission from the coronal part because the footpoints of these loops are located behind the solar limb.

The EBTEL code is publicly accessible at https://github.com/rice-solar-physics/EBTEL. The main program is called ebtel2.pro, which computes the evolution of spatially averaged loop quantities using the above simplified equations. Combined with the CHIANTI atomic database (Dere et al. 1997, 2009), the routine—intensity_ebtel.pro—computes the line intensity as a function of time.
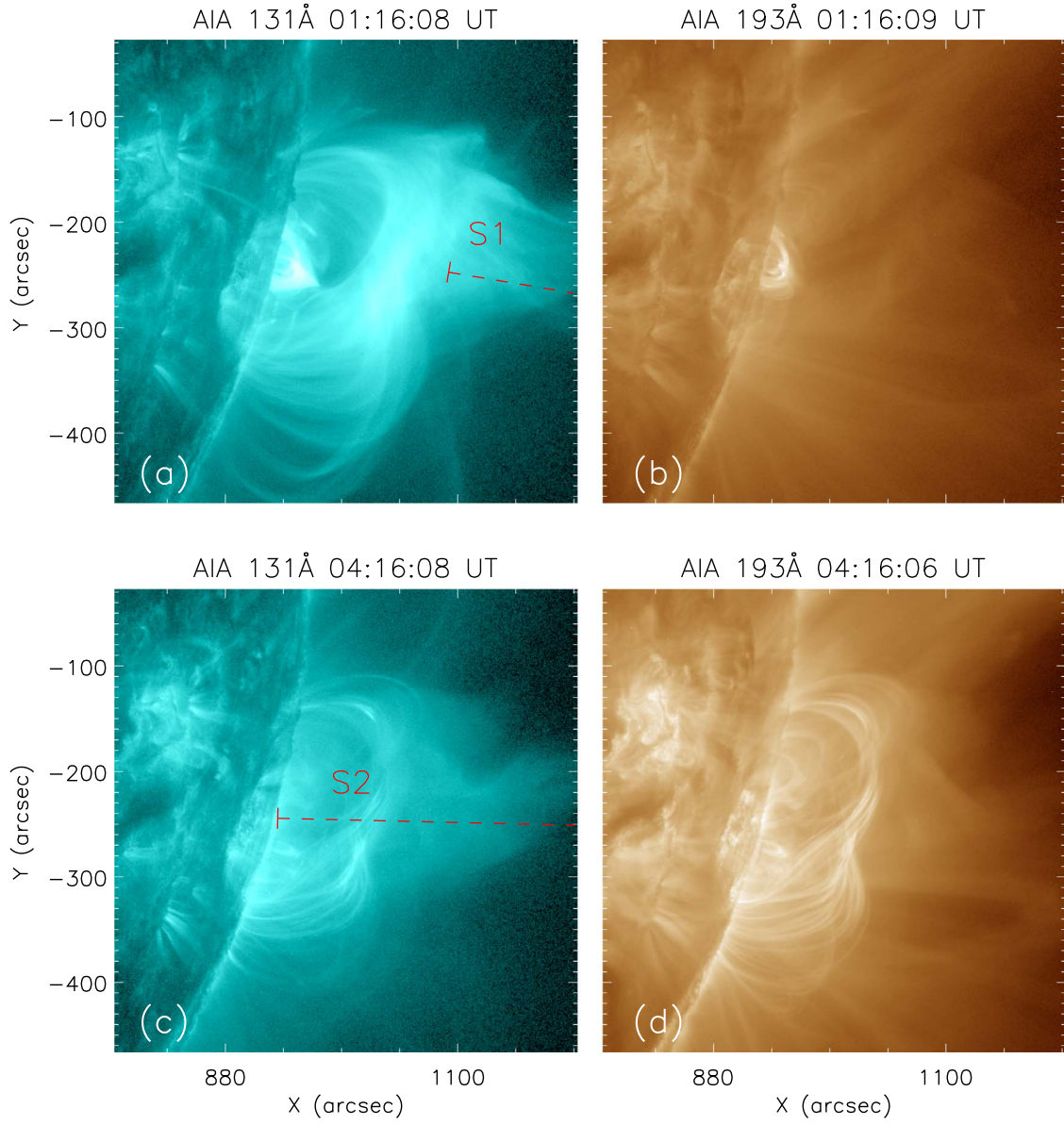
Figure 3. Morphology and thermodynamics evolution during the late phase. Panel (a) shows the cusp structure at the top of late-phase loops in AIA 13.1 nm, but in panel (b) only the post flare loops from the main-phase region could be seen in AIA 19.3 nm. Panels (c) and (d) show that when these late-phase loops cool down, in AIA 13.1 and 19.3 nm we can see large arcade loops overlying at the top. Here we consider that the observations in AIA 13.1 nm in panel (c) mainly come from the Fe VIII line emission (0.4 MK), which is blended in AIA 13.1 nm. The animation begins at 00:06:07 UT and ends at 08:56:07 UT. Its duration is 11 s.

(An animation of this figure is available.)

3.4.2. EBTEL-based Flare Model

There are three steps to calculating the line emission based on the EBTEL model. First, for each single loop, the EBTEL program gives the differential emission measure (DEM) as a function of time and temperature. The inputs of the model are heating function, $Q(t)$ (erg cm^{-3} s^{-1}) and loop half length (cm). The heating function has a linear slope, i.e.,

$$Q(t) = \begin{cases} Q_{\mathrm{bkgd}} + Q_0 + \dfrac{2Q_0}{dt}(t - t_0) & \text{if } t_0 - \dfrac{dt}{2} < t < t_0, \\ Q_{\mathrm{bkgd}} + Q_0 - \dfrac{2Q_0}{dt}(t - t_0) & \text{if } t_0 \leqslant t < t_0 + \dfrac{dt}{2}, \end{cases}$$

(4)

where Q_0 is the heating amplitude; dt is the heating duration, which is set to be the interval between two time-adjacent loops, namely 11.2 minutes; and Q_{bkgd} is the background heating at a low level of 10^{-6} erg cm^{-3} s^{-1}. The initial setting is similar to that in Hock et al. (2012) except that here we fix the start time of the heating (t_0) for each loop based on observations:

$$t_0 = t_0' + i \times dt,$$

(5)

where t_0' is the first episode of the late-phase heating. As the reconnection continues, higher reconnected loops will shrink backward, and the half length of these loops, l, will increases. Here we simply assume a linear increase in length of consecutive loops and a linear decrease in the heating magnitude.
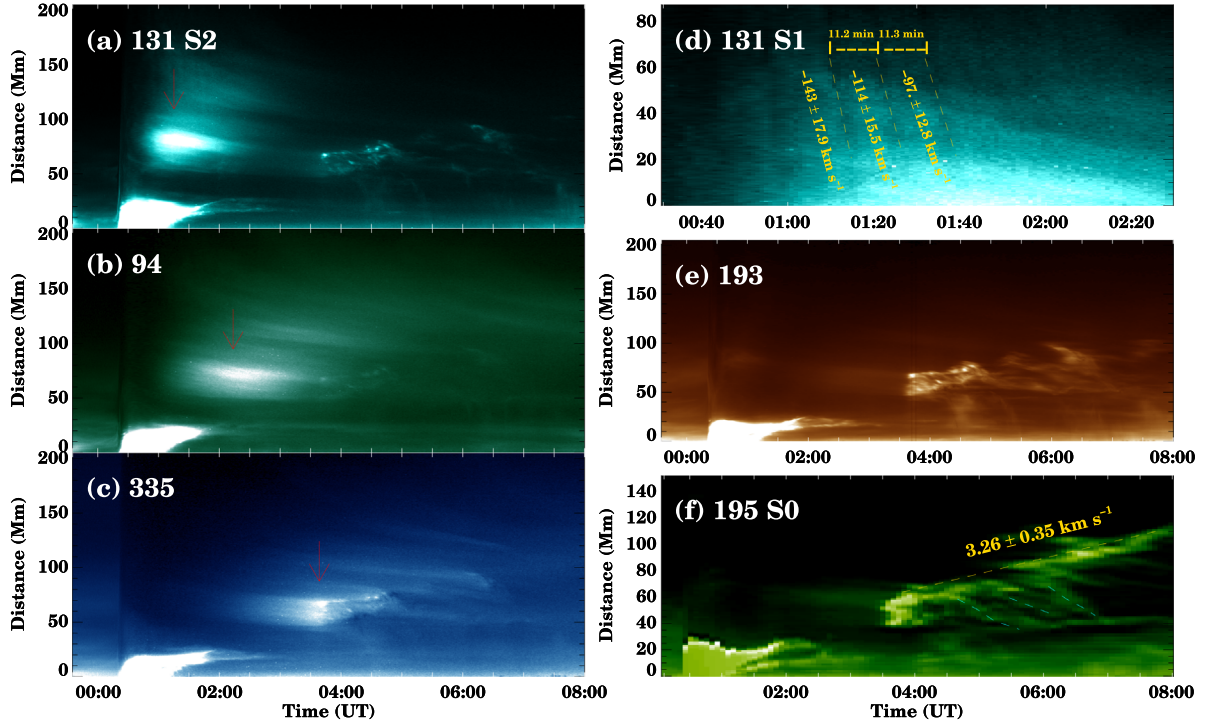
Figure 4. Slice–time stacking plots for slits S0–S2. (a)–(c) and (e) S2 plots at AIA 13.1, 9.4, 33.5, and 19.3 nm capture the evolution of the late-phase loops. (d) The S1 plot captures the center of the cusp structure. (f) S0 plot at EUVI_B 19.5 nm provides another viewing angle to see the evolution of the late-phase loops. The vertical arrows point out the brightness moments and the horizontal arrows mark the duration of brightness in each plot.

Table 2
Late-phase Parameters for the EBTEL-based Flare Model

	Parameters	Our Model	Hock Model	Note
Single loop parameters	l^*	$l_0' + i \times \Delta l$	free	Loop half length (cm)
	$t0$	$t_0' + i \times \Delta t$	free	Time of peak impulsive heating (s), $\Delta t = 672$ s
	dt	672 s	300 s	Duration of heating (s)
	$Q0$	$Q_0' + i \times \Delta h$	free	Amplitude of heating (erg cm^{-3} s^{-1})
	A	free	free	Loop cross-section area (cm^2)
Global parameters	N_{loops}	10	22	Number of EBTEL loops
	C	3.56×10^{-27}	3.56×10^{-27}	Normalization factor (sr m^{-2})

Note. The loop half length (l^*) is a free parameter that is constrained using the imaging observations, l_0', t_0', and Q_0', which are also free parameters. Numbers of loops for our model are estimated from observation.

EBTEL will return DEM_COR(t, T) (DEM from the corona part) and DEM_TR(t, T) (DEM from the transition region). Due to the occulting effect of the solar limb, here we only need to calculate the emission from the corona. The line radiance is the convolution of the DEM with the contribution function $G(T)$ that contains abundance factor, i.e.,

$$I_{\text{loop}}(t) = \int_T \text{DEM}(t, T) G(T) dT. \qquad (6)$$

Note that the contribution function is calculated by the program gofnt.pro in the CHIANTI package.

At last, the total emission of the late phase is generated by combining the contribution of all EBTEL loops. To compare with EVL data, a constant normalization factor C is used to convert the radiation at the Sun to the irradiance received at Earth (1 au) assuming a uniform (constant) angular distribution

of flare energy release, as shown below:

$$E_{\text{model}}(t) = C \sum_{i=1}^{N_{\text{loops}}} A_i I_{\text{loop},i}(t), \qquad (7)$$

and

$$C = \left(0.001 \frac{\text{W m}^{-2}}{\text{erg cm}^{-2} \text{ s}^{-1}}\right) d\Omega, \qquad (8)$$

where A_i is the loop cross-section area, which is the same for the modeling loops. N_{loops} is the number of the loops, and $d\Omega$ (3.56×10^{-24} sr m^{-2}) is the solid angle subtended by 1 m^2 at 1 au, which yields a normalization factor C of 3.56×10^{-27} (Hock 2012). All parameters in the EBTEL-based flare model are listed in Table 2.
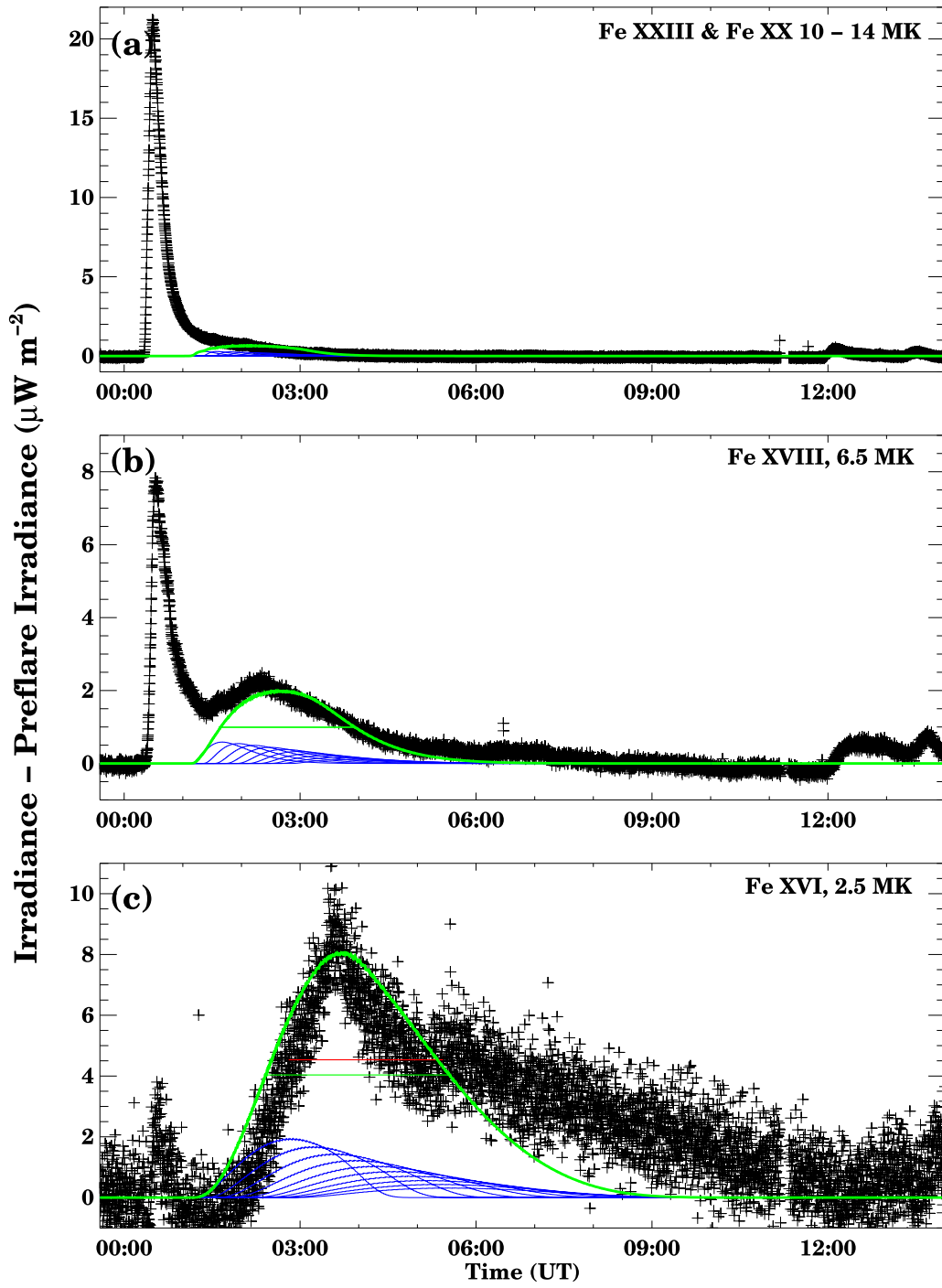
Figure 5. Results of the EBTEL-based flare model for both the Fe XVIII (middle) and the Fe XVI line (bottom). The observation and modeling of the Fe XX/XXIII blended line are placed on the top just for reference. The pluses are the EVE observations with the preflare background irradiance subtracted off. The blue lines represent the contribution from each individual coronal loop strand and the green line is the output from the model.

Table 3
Comparison of Properties from Observations and Modelings

Passband	Ion	Temperature	Observation			Modeling		
			Peak Intensity	Peak Time	FWHM	Peak Intensity	Peak Time	FWHM
(nm)		(MK)	(μW)	(UT)	(minutes)	(μW)	(UT)	(minutes)
9.4	Fe XVIII	6.5	2.000	02:26:02	*	1.985	02:39:02	140
33.5	Fe XVI	2.5	9.071	03:31:42	158	8.071	03:42:32	192

3.4.3. Modeling Result

Using the EBTEL-based flare model, we reproduce the irradiance in different emission lines for the late-phase loop system and compare it with EVE's observations (Figure 5). The late-phase emission in the hot line (13.3 nm, >10 MK) could barely be seen as the late-phase emission is largely submerged under main-phase emission. This blending effect also affects the 9.4 nm EVE line, resulting in an obvious overlapping of the main-phase and late-phase emissions during 01:00 UT to 02:00 UT (as shown by the black line in Figure 5(b)). Thus we only use the 9.4 nm data after 02:00 UT to do the fitting. As for 33.5 nm line irradiance, the late-phase bump is clearly identified.

We fit both 9.4 and 33.5 nm lines using the MPFIT package. The result shows a good agreement between the observations and modeling (Figure 5 and Table 3). The observed 13.3 nm emission and modeled one are plotted in the top panel of Figure 5. The best-fit gives an initial loop half length (l'_0) of 179 Mm and heating rate (Q'_0) of 0.022 erg cm^{-3} s^{-1}, which is comparable to that in Hock et al.'s (2012) model ($\sim$0.01 erg cm^{-3} s^{-1}), but less than that (0.2 erg cm^{-3} s^{-1}) of case 1 in Li et al. (2012) by one order of magnitude. However, in Li et al.'s (2012) model, only one loop was used to model the late-phase loop. the best-fit loop cross-section is 1.3×10^{16} cm^2 corresponding to a loop width of 1.3 Mm.

Using the EBTEL model, we reconstruct the irradiance of the flare late phase and study the role of additional heating in the appearance of an EUV late phase. Our results show that the late-phase peak times in observations and modeling for each line are very close to each other (within 15 minutes). Hence the long delay appearing in the warm lines can be well explained. Liu et al. (2013a) estimated the cooling time of the late-phase loop arcade by using the formula derived by Cargill et al. (1995) based on a simple cooling model:

$$\tau_{\rm cool} \doteq 2.35 \times 10^{-2} l^{5/6} T_e^{-1/6} n_e^{-1/6}. \tag{9}$$

The parameters l, T_e, and n_e are, respectively, the loop half length, electron temperature, and electron density at the beginning of the cooling. Here we use the best-fit loop half length (179 Mm) as the input. The temperature and density are determined using DEM analysis (Schmelz et al. 2011; Cheng et al. 2012). The derived initial temperature of the late phase is 14 MK and density is $\sim$6 $\times$ 10^9 cm^{-3}. These parameters yield a cooling time around 210 minutes. However, the delay time of the late-phase peak (at 05:00 UT) in Fe IX 17.1 nm (0.7 MK) is about 280 minutes. The late appearance of the late-phase loop arcade in the EUV band is mainly a cooling-delay effect with additional consecutive heating.

4. Summary and Discussion

In summary, we examine an extremely large late phase during an eruptive solar flare. The magnetic topology is a quadrupolar magnetic configuration, which facilitates the coexistence of lower core field and a high large-scale overlying field. The cusp structure observed in the hot channel evidences the occurrence of the magnetic reconnection process (Tsuneta et al. 1992; Aschwanden 2005), and the downward motion of the hot loops represents the shrinkage of newly formed loops (Forbes & Acton 1996). All these observations suggest the possibility of magnetic reconnection taking place high above.

Such a reconnection process is caused by the erupting CME. The overlying arcades are stretched upward by the CME, and the stretched field lines reclose after the reconnection beneath the CME. This process, similar to the tether-cutting reconnection, happens in the late-phase stage. It provides additional heating mechanism for the EUV late phase. The detailed evolution for the late-phase loop system is described as follows:

1. Before the flare, the large-scale overlying arcades connect the outer positive and negative polarities. The quadrupolar magnetic configuration distinguishes the overlying arcades from the lower core field.
2. When the CME erupts, the overlying arcades are stretched outward and the tether-cutting-like reconnection takes place between two legs of the overlying field. The reconnection plays two roles: magnetic topology is rearranged and magnetic energy is converted to additional heating that is transferred into the late-phase loop system.
3. As the reconnection continues, the cusp structure retreats backward and shows some quasiperiodic characteristics.
4. As time goes on, these loops cool down and become visible in the low temperature lines, such as the AIA 19.3 nm and EUVI 19.5 nm. Because inner loops form first and then cool down first, like the PFL systems, the loop top shows a rising motion.

As a summary, we consider that the late-phase emission comes from a set of gradually downward moving loops rather than a pre-existing loop system. The observational features also imply the existence of additional heating of the large-scale flare loops, which is shown in the bottom panel of Figure 2.

We also use EBTEL to model the EVE irradiance in several lines. The modeling result shows good agreement with the observations. The peak time in each line is very close to the observations, indicating that additional heating gives rise to the delayed appearance of the late phase.

Liu et al. (2015) and Wang et al. (2016) argued that the extremely large late-phase emission caused the energy redeposition from the failed flux rope leading to the thermal emissions, whereas Dai et al. (2018) presented a more complicated scenario in their case: the late-phase loops are mainly produced by the first-stage QSL reconnection, while the second-stage reconnection is responsible for the heating of main flaring loops. However, the production of extremely large EUV late phase in this flare is from the late-phase reconnection occurring high above the main flare region. The CME originating from main flare is only the trigger.

ORCID iDs

Zhenjun Zhou
 (周振军) ● https://orcid.org/0000-0001-7276-3208
Xin Cheng ● https://orcid.org/0000-0003-2837-7136
Lijuan Liu ● https://orcid.org/0000-0001-6804-848X
Yu Dai ● https://orcid.org/0000-0001-9856-2770
Yuming Wang ● https://orcid.org/0000-0002-8887-3919
Jun Cui ● https://orcid.org/0000-0002-4721-8184

References

Antiochos, S. K., & Sturrock, P. A. 1978, ApJ, 220, 1137
Aschwanden, M. J. 2005, Physics of the Solar Corona. An Introduction with
    Problems and Solutions (2nd ed.; Chichester: Praxis Publishing Ltd.)
Brueckner, G. E., Howard, R. A., Koomen, M. J., et al. 1995, SoPh, 162, 357
Bumba, V., & Krivský, L. 1959, BAICz, 10, 221
Cargill, P. J., Bradshaw, S. J., & Klimchuk, J. A. 2012, ApJ, 752, 161
Cargill, P. J., Mariska, J. T., & Antiochos, S. K. 1995, ApJ, 439, 1034
Chen, Y., Du, G., Zhao, D., et al. 2016, ApJL, 820, L37
Cheng, C. C., Pallavicini, R., Acton, L. W., & Tandberg-Hanssen, E. 1985,
    ApJ, 298, 887
Cheng, X., Zhang, J., Saar, S. H., & Ding, M. D. 2012, ApJ, 761, 62
Contarino, L., Romano, P., Yurchyshyn, V. B., & Zuccarello, F. 2003, SoPh,
    216, 173
Dai, Y., & Ding, M. 2018, ApJ, 857, 99
Dai, Y., Ding, M., Zong, W., & Yang, K. E. 2018, ApJ, 863, 124
Dai, Y., Ding, M. D., & Guo, Y. 2013, ApJL, 773, L21
Dere, K. P., Landi, E., Mason, H. E., Monsignori Fossi, B. C., & Young, P. R.
    1997, A&AS, 125, 149
Dere, K. P., Landi, E., Young, P. R., et al. 2009, A&A, 498, 915
Fárník, F., Hudson, H., Karlický, M., & Kosugi, T. 2003, A&A, 399, 1159
Forbes, T. G., & Acton, L. W. 1996, ApJ, 459, 330
Gallagher, P. T., Dennis, B. R., Krucker, S., Schwartz, R. A., & Tolbert, A. K.
    2002, SoPh, 210, 341
Hock, R. A. 2012, PhD thesis, Univ. Colorado
Hock, R. A., Woods, T. N., Klimchuk, J. A., Eparvier, F. G., & Jones, A. R.
    2012, arXiv:1202.4819
Hudson, H. S. 2011, SSRv, 158, 5
Kaiser, M. L., Kucera, T. A., Davila, J. M., et al. 2008, SSRv, 136, 5
Klimchuk, J. A., Patsourakos, S., & Cargill, P. J. 2008, ApJ, 682, 1351
Lemen, J. R., Title, A. M., Akin, D. J., et al. 2012, SoPh, 275, 17
Li, Y., Ding, M. D., Guo, Y., & Dai, Y. 2014, ApJ, 793, 85
Li, Y., Qiu, J., & Ding, M. D. 2012, ApJ, 758, 52
Liu, K., Wang, Y., Zhang, J., et al. 2015, ApJ, 802, 35
Liu, K., Zhang, J., Wang, Y., & Cheng, X. 2013a, ApJ, 768, 150
Liu, W.-J., Qiu, J., Longcope, D. W., & Caspi, A. 2013b, ApJ, 770, 111
Martin, S. F. 1980, SoPh, 68, 217
Masson, S., Pariat, É., Valori, G., et al. 2017, A&A, 604, A76
McKenzie, D. E., & Hudson, H. S. 1999, ApJL, 519, L93
Pesnell, W., Thompson, B., & Chamberlin, P. 2012, SoPh, 275, 3
Qiu, J., Liu, W.-J., & Longcope, D. W. 2012, ApJ, 752, 124
Schmelz, J. T., Worley, B. T., Anderson, D. J., et al. 2011, ApJ, 739, 33
Stenborg, G., Vourlidas, A., & Howard, R. A. 2008, ApJ, 674, 1201
Sterling, A. C., & Moore, R. L. 2004, ApJ, 613, 1221
Sun, X., Hoeksema, J. T., Liu, Y., et al. 2013, ApJ, 778, 139
Thompson, W. T. 2009, Icar, 200, 351
Tsuneta, S., Hara, H., Shimizu, T., et al. 1992, PASJ, 44, L63
Van Hoven, G., & Hurford, G. J. 1984, AdSpR, 4, 95
Wang, Y., Zhou, Z., Zhang, J., et al. 2016, ApJS, 223, 4
Warren, H. P., & Warshall, A. D. 2001, ApJL, 560, L87
Woods, T. N., Eparvier, F. G., Hock, R., et al. 2012, SoPh, 275, 115
Woods, T. N., Hock, R., Eparvier, F., et al. 2011, ApJ, 739, 59
Woods, T. N., Kopp, G., & Chamberlin, P. C. 2006, JGRA, 111, A10S14
Zhou, Z., Zhang, J., Wang, Y., Liu, R., & Chintzoglou, G. 2017, ApJ, 851, 133